ACS OMEGA

http://pubs.acs.org/journal/acsodf

Article

Effect of (Sm, In) Doping on the Electrical and Thermal Properties of Sb_2Te_3 Microstructures

Nitasha Komal, Muhammad Adil Mansoor, Muhammad Mazhar, Manzar Sohail,* Zahida Malik,* and Muhammad Anis-ur-Rehman

Cite This: *ACS Omega* 2023, 8, 9797−9806

Read Online

ACCESS | Metrics & More | Article Recommendations

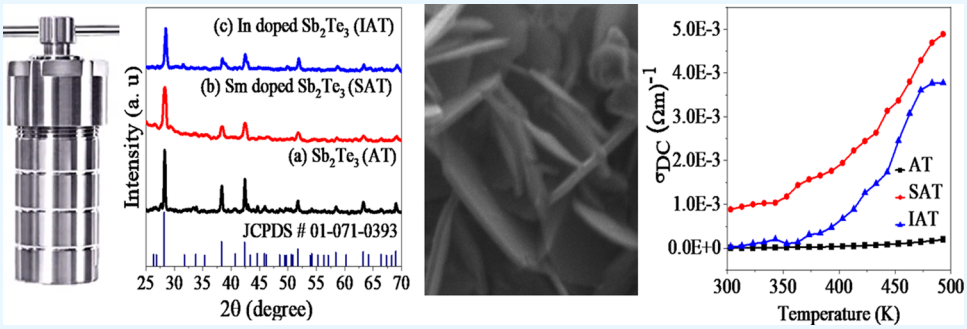

ABSTRACT: Doped Sb_2Te_3 narrow-band-gap semiconductors have been attracting considerable attention for different electronic and thermoelectric applications. Trivalent samarium (Sm)- and indium (In)-doped Sb_2Te_3 microstructures have been synthesized by the economical solvothermal method. Powder X-ray diffraction (PXRD) was used to verify the synthesis of single-phase doped and undoped Sb_2Te_3 and doping of Sm and In within the crystal lattice of Sb_2Te_3. Further, the morphology, structure elucidation, and stability have been investigated systematically by scanning electron microscopy (SEM), Raman analysis, and thermogravimetric analysis (TGA). These analyses verified the successful synthesis of hexagonal undoped Sb_2Te_3 (AT) and (Sm, In)-doped Sb_2Te_3 (SAT, IAT) microstructures. Moreover, the comparison of dielectric parameters, including dielectric constant, dielectric loss, and tan loss of AT, SAT, and IAT, was done in detail. An increment in the electrical conductivities, both AC and DC, from 1.92×10^{-4} to 4.9×10^{-3} Ω^{-1} m^{-1} and a decrease in thermal conductivity (0.68−0.60 W m^{-1} K^{-1}) were observed due to the doping by trivalent (Sm, In) dopants. According to our best knowledge, the synthesis and dielectric properties of (Sm, In)-doped and undoped Sb_2Te_3 in comparison with their electrical properties and thermal conductivity have not been reported earlier. This implies that appropriate doping with (Sm, In) in Sb_2Te_3 is promising to enhance the electronic and thermoelectric behavior.

1. INTRODUCTION

It has been well reported that different electronic properties can be induced in chalcogenides by doping different metals. The resulting semiconductor chalcogenides with nano and microstructures have been employed in different applications such as optoelectronics, supercapacitors,[1] and thermoelectric (TE),[2,3] and photoelectric devices.[4] Among these semiconductors, antimony telluride (Sb_2Te_3) is a well-studied chalcogenide for many emerging applications, including thermoelectric,[5] thermopile sensors,[6] phase-change memory devices,[7] and electronic appliances.[8] Moreover, antimony telluride (Sb_2Te_3) is a narrow-band semiconductor and is considered an outstanding material for thermoelectric applications at room temperature.[9] Thermoelectric properties predominantly depend on the electric and thermal behavior of the material.[10] Up to now, different strategies, including composite formation,[11] doping,[12] and synthesis of sandwich structures,[13] have been employed to improve the electric and thermal properties of Sb_2Te_3 for thermoelectric applications. Among all of these methods, the addition of dopants is a convenient and facile approach to get the required properties.[14] Recently, doping by various dopants such as Ag,[15] Se,[16] W,[17] and V[18] in Sb_2Te_3 films has been reported for enhanced thermoelectric and phase-change memory applications. Bi-doped Sb_2Te_3 films have been reported by Fan and his co-workers. They investigated the effect of Bi doping on the structural and thermoelectric properties of Sb_2Te_3.[19] Sulfur-doped Sb_2Te_3 has also been explored theoretically[13] and

Received: September 9, 2022
Accepted: December 9, 2022
Published: March 10, 2023

experimentally[20] for enhancing the electrical properties of Sb_2Te_3. To date, although addition of various dopants in Sb_2Te_3 structures has been reported and their effect on different properties has been investigated, doping of rare earth elements and group III A has not been much explored. We have chosen samarium (Sm) and indium (In) as dopants, as considerable work has been done to study their effect on various properties as dopants in different materials except Sb_2Te_3.[22,23] During the last decade, trivalent Sm-doped Fe_2O_3 nanomaterials have been prepared and studied for improved magnetic and supercapacitive applications.[23] Furthermore, samarium as dopant also exhibits improved electronic,[24] photocatalytic degradation under visible light[24] and solar cell applications.[25] In addition, Sm^{+3}-doped chalcogenides, including $Se_{95}Te_5$,[26] As-Se-Te,[27] and As-Se-S,[27] have been prepared and studied for better thermal stability and ultra-fast phase-changing memory devices. Similarly, In as dopant has been well explored as a photocatalyst,[28] and for photovoltaic,[29] photoelectrochemical,[30] and electrochemical properties,[31] as well as for enhanced gas-sensing application.[32,33] Moreover, different In-incorporated chalcogenides like Se-Te-In,[34] GeTe,[35] and Cu-Cr-Se[36] have been studied in detail for their superior thermoelectric and optoelectronic properties. Different approaches including electrodeposition,[37] magnetron sputtering,[38] solid-state reaction method,[16] and solvothermal method[13] have been developed for synthesis of doped Sb_2Te_3 materials. In this study, solvothermal is the approach of choice because of it being economic, handy, and of better yield.

As is noticeable from literature, Sm and In as dopants have imparted a considerable impact on the properties of different materials, particularly chalcogenides, but the synthesis of Sm and In-doped Sb_2Te_3 microstructures and their effect on electrical and thermal properties have never been described previously. Consequently, the aim of this work is to present the synthesis of Sm-doped Sb_2Te_3 (SAT) and In-doped Sb_2Te_3 (IAT) microstructures by the convenient solvothermal approach and further elaborate the effect of Sm and In addition as dopants on the electrical and thermal properties of Sb_2Te_3 microstructures. Moreover, the prepared materials have been characterized by powder X-ray diffraction (PXRD), scanning electron microscopy (SEM), energy-dispersive spectroscopy (EDS), Raman spectroscopy, and TGA, while the electrical behavior, thermal conductivity, and other related parameters of all of the synthesized materials have also been explained thoroughly.

2. RESULTS AND DISCUSSION

X-ray powder diffraction data was obtained for as-casted and dried samples using a Bruker D8 advanced system with Cu $K\alpha_1$ monochromatic radiation (λ = 0.1542 nm) and 2θ values of 25−70° at 40 kV. The powder diffractograms were compared using the PDF database given by ICDD for preliminary phase confirmation. A visual comparison of the powder patterns has been done by utilizing the Origin software.[31] To find out the morphologies, structural hierarchy, and elemental composition of the materials, SEM by electron probe microanalysis (EPMA) using a TESCAN VEGA 3 LMU equipped with an EDX system operated at 10 kV was employed over the samples coated by standard procedures. The vibrational structural aspects of the prepared materials were investigated by Raman analysis using μ-Raman-532 TEC-Ci. A small amount of thoroughly grinded powder was placed on a glass slide for analysis. The thermal behaviors of doped and undoped Sb_2Te_3 were studied by TGA using a DTG-60H simultaneous DTA-TG system by SHIMADZU, fitted with an alumina crucible, with ±0.005% accuracy. The sample holder containing the sample was thermally treated from 298 to 973 K at the rate of 10 K min^{-1} under ambient dinitrogen. The material was pelletized by a hydraulic press at a pressure of 1000 Pa and these pellets were annealed at 523 K for 3 h. Afterwards, their dielectric behavior was measured by an LCR meter (Wayne Kerr 6440B); DC analysis was performed from 300 to 500 K by employing a two-probe system. The same pellets were used for temperature-dependent (298−393 K) thermal conductivity measurements by using a thermal constant analyzer (TPS 2500 S). The transient plane source technique is an advanced and effective method for studying the thermal transport properties of materials by considering the sample both as a heat source and as a temperature sensor.[39−41] This method based on three-dimensional heat flow in the sample is used to calculate the different thermal transport parameters by fitting of experimental data.

2.1. Powder X-Ray Diffraction (PXRD). The powder PXRD patterns of prepared Sb_2Te_3 (AT), Sm-doped AT (SAT), and In-doped AT (IAT) samples are provided in Figure 1. The PXRD peaks of AT show the formation of a

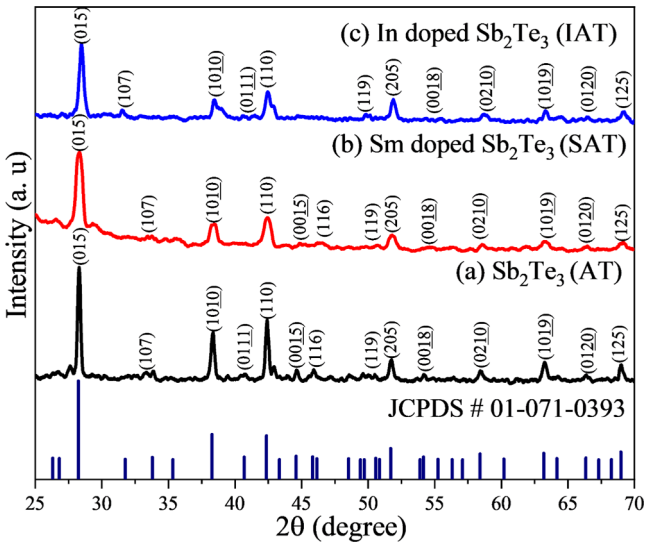

Figure 1. PXRD patterns of (a) AT (black), (b) SAT (red), and (c) IAT (blue) compared with JCPDS card no. (01-071-0393). For all of the three XRD patterns, different *hkl* lattices at the corresponding peaks are added.

rhombohedral phase (JCPDS file no.: 01-071-0393)[25,26] with space group (no:166) $R\bar{3}m$. Comparable XRD patterns of Sb_2Te_3 have also been reported by Shi et al. for nanoplates[42] and by Dong et al. for other nanoforms.[43] Furthermore, the variation in position (2θ values of 0.25−0.5) of the peaks by addition of Sm and In verifies the substitution of dopants within the lattice of Sb_2Te_3. The broadness of peaks was observed along (015), (107), (10$\underline{1}$0), (01$\underline{1}$1), (116), and (00$\underline{1}$8) in the case of SAT, which may be due to the formation of smaller grains by the addition of Sm. A peak shift is evident due to enhanced lattice parameters as a result of Sm (1.098 Å) doping instead of Sb (0.9 Å) in the lattice. In the case of IAT, the atomic radius of In (0.94 Å) was responsible for the peak shift and the obvious peak broadening was due to decrease in crystallinity; the smallest crystallite size of IAT among all the

https://doi.org/10.1021/acsomega.2c05859
ACS Omega 2023, 8, 9797−9806

three samples is shown in Table 1. It may be because of the substitution of In within the crystal lattice of Sb_2Te_3 leading to

Table 1. Average Crystallite Sizes of Doped and Undoped Sb_2Te_3 Calculated by Scherrer Formula

sample	microstructures	average crystallite grain size (nm)	peak position 2θ (degree)
AT	Sb_2Te_3	72	28.34
SAT	Sm-doped Sb_2Te	68	28.28
IAT	In-doped Sb_2Te_3	42	28.51

deformation of the hexagonal structure and suppressing the growth of crystallites. For both SAT and IAT, a precise test for intermetallic secondary phases such as SmSb, SmTe, InSb, and InTe has been carried out; none was noticeable except the desired Sb_2Te_3. Moreover, there is no oxide and unreacted tellurium impurity phases have been observed in XRD after annealing of the prepared chalcogenide samples at 753 K under a H_2/Ar mixture, as shown in Figure 1.

The crystallite grain sizes of doped and undoped Sb_2Te_3 microstructures were also calculated for major XRD peaks by using Scherrer formula[44] as given below

$$D = \frac{0.94\lambda}{B\cos\theta}$$

where 0.94 is a constant, λ is the wavelength of the incident X-ray, i.e., 0.1542 nm, B is the full width at half-maxima (FWHM), and θ is Bragg diffraction angle (radians). The calculated values of crystallite grain size of all prepared microstructures are provided in Table 1. The decrease in crystallite size was observed in SAT and IAT, which indicates that the dopants restrict the growth of grains and consequently reduce the grain size.[38]

2.2. Morphological and Elemental Analysis. The structural and elemental analyses of the prepared samples have been carried out by SEM equipped with EDS. Figure 2 shows the images of prepared pristine Sb_2Te_3- (Figure 2a), Sm- (Figure 2b), and In-doped (Figure 2c) Sb_2Te_3 microstructures. Figure 2a shows the rod-like growth of pure Sb_2Te_3; however, Sm-doped Sb_2Te_3 shows the formation of hexagonal discs of agglomerated particles, while indium-doped Sb_2Te_3 shows a mixed morphology of hexagonal discs and rods. This confirms that different dopants cause the nucleation and growth process in different fashions and lead to variation in crystallite size, particle size, and morphology, as is evident from the XRD results, which show that doped Sb_2Te_3 has smaller crystallite size than the undoped one.[45] Smaller grains or crystallites have less surface free energy, which assists the agglomeration and enhances the nucleation, and hence they tend to grow in larger particles, as observed in the case of SAT, where hexagonal discs were formed. However, in the case of IAT, both hexagonal and rod-shape morphologies were found. Although the crystallite size of In is the smallest (42 nm) and leads to the formation of larger hexagonal discs similar to SAT, as discussed in Section 2.1, the atomic radius of In is smaller than Sm and comparable to Sb, which could suppress the nucleation and lead to the preferential growth of rods, as observed in the AT microstructures provided in Figure 2a.

Moreover, EDX analysis confirms the uniform distribution of dopants within the flakes of Sb_2Te_3. The quantitative atom % of dopants in the Sb_2Te_3 microstructures obtained from EDX analysis is shown in Table 2. Furthermore, EDS results also revealed the presence of some oxygen impurity, which might be due to the adsorbed oxygen in the vacancies of the microstructures.

Table 2. Quantitative Atom % for SAT and IAT

sample type	composition (atom %)
AT	Sb_2Te_3
SAT	$(Sb_2Te_3)Sm_{4.3}$
IAT	$(Sb_2Te_3)In_{4.1}$

2.3. Raman Spectroscopic Analysis. Raman spectroscopy was used to elucidate the vibrational structure of chalcogenides via phonon interactions. The Raman spectra of the pristine Sb_2Te_3 microstructure, SAT, and AT in the range of 100−300 cm^{-1} are provided in Figure 3. The Raman active

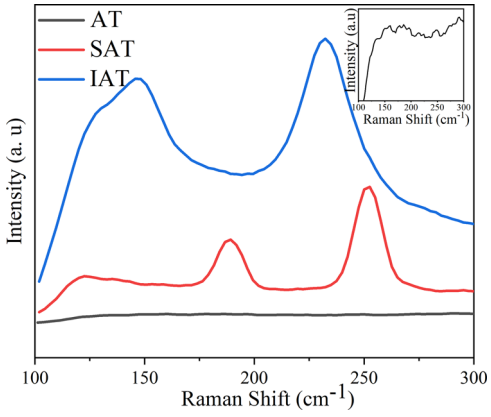

Figure 3. Raman vibrational modes of prepared AT, SAT, and IAT microstructures. The inset shows the enlarged view of AT.

phonon vibrations of Sb_2Te_3 microstructures are observed at 108, 119, 135, and 162 cm^{-1}, which correspond to A_{1g} (1), E_g (1), A_{1g} (2), and E_g (2) modes, respectively.[21,30] Further, Figure 3 also depicts that IAT microstructures show a phenomenon of blue shift for Raman active modes of Sb_2Te_3. But in the case of Sm doping, a red shift was observed for Sb_2Te_3 Raman active vibrational bands. The phenomena of

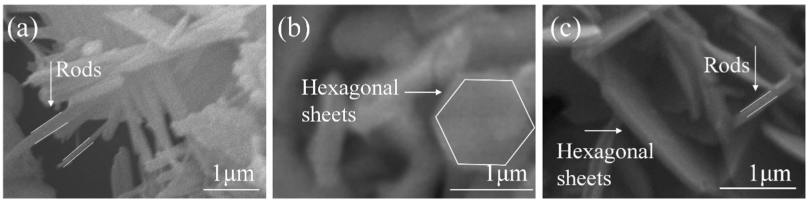

Figure 2. SEM micrographs of prepared (a) AT microstructures, (b) SAT microstructures, and (c) is IAT microstructures.

https://doi.org/10.1021/acsomega.2c05859
ACS Omega 2023, 8, 9797−9806

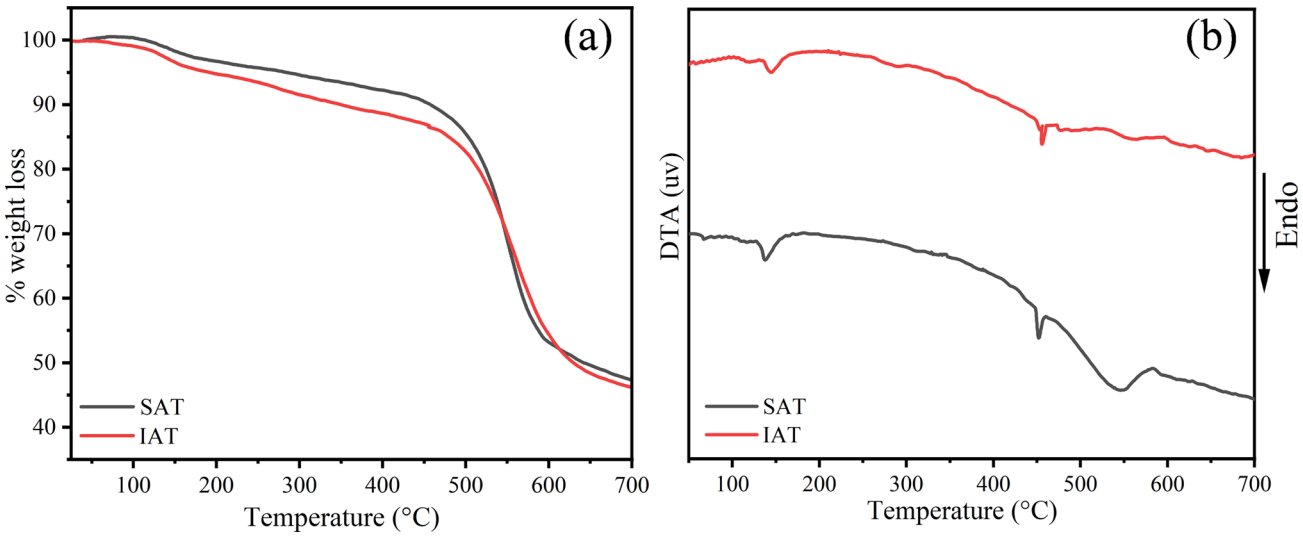

Figure 4. (a) % weight loss as a function of temperature of all doped Sb_2Te_3 microstructures; (b) DTA behaviors of SAT and IAT.

red and blue shifts were observed due to the existence of the dopant and also because of variation in the crystallite size of the prepared doped and undoped Sb_2Te_3.[31−33] The decreases in crystallite size are symmetrically related to the peak broadness and occurrence of blue shift.[48] Additionally, this result also corresponds to the PXRD pattern of the prepared materials. As is evident from Figure 3, the bands width of IAT are greater than those of SAT and AT, which correlate with the higher FWHM of IAT. As discussed earlier in Section 4.1, FWHM is inversely related to the crystallite size of the material; hence, IAT has a smaller crystallite size compared to AT and SAT,[49] as shown by the results of peak broadness and blue shift in IAT. Furthermore, there is absence of any oxide band, as indicated from Figure 3, which verifies the purity of the prepared doped materials.

2.4. Thermal Analysis (TGA). The thermal stability of SAT and IAT was studied by TGA. Figure 4 shows the two-step weight loss thermogram of all prepared microstructures. In all samples, at about 397 K a small weight loss of 3% was noticed, which is due to the removal of adsorbed water vapors.[50] Further, a major second step weight loss was observed at 738−883 K, which is attributed to the vaporization of Te and melting of Sb_2Te_3[51−53] in all prepared samples. In both cases, after neglecting the water loss, TGA curves can be attributed as a single-stage decomposition. Moreover, the DTA analyses of both doped prepared samples are given in Figure 4b. The DTA plots of SAT and IAT closely resemble the TGA behavior of these materials. The 1st endotherm appearing below 423 K corresponds to the evaporation of the adsorbed water, while the 2nd and 3rd endotherms observed at 723−733 and 823−833 K correspond to the melting of excess chalcogenide and Sb_2Te_3 melting. Therefore, we can conclude that SAT and IAT show comparable thermal behaviors and no significant change in the melting point of Sb_2Te_3 was observed by addition of Sm and In as dopants. Further TGA results also confirm the absence of any oxide impurity in the prepared doped Sb_2Te_3, as no weight loss was observed from 473 to 573 K, which corresponds to Sb_2O_3 decomposition.[36,37]

2.5. Electrical Properties of Doped and Undoped Sb_2Te_3. The dielectric and conducting properties of as-synthesized materials were investigated and are discussed below.

2.5.1. Dielectric Studies. Dielectric studies give an idea about the electrical energy storage capacity of the material by electrical polarization. We measured the dielectric properties of the prepared doped and undoped Sb_2Te_3 microstructures at room temperature within the frequency range of 20 Hz to 3 MHz.

The real part of the dielectric provides information about the storing capability of the electrical energy, while the imaginary part reveals the loss of stored electrical energy. Figure 5a shows the dependence of the real part of the dielectric constant (ε') on the frequency for all prepared AT, SAT, and IAT. The decrease in dielectric constant was observed with increase in frequency. A sharp decline in ε' was noticed at lower frequencies as compared to higher frequencies, which is similar to the usual behavior of dispersion reported in dielectrics.[54] In dielectric materials, four types of polarizations, i.e., atomic, electronic, ionic, and interfacial, are present, which are responsible for the variation in dielectric constant. At low frequencies, the value of dielectric constant is higher because all four types of polarization take part but interfacial polarization comes into contact mainly. As the frequency increases, the polarization decreases and reaches a constant value because the atoms have not enough time to align themselves along with the alternating field.[55] Moreover, the phenomenon of hopping is also responsible for the higher dielectric constant at lower frequencies. In this case, the value of dielectric constant was decreased by the addition of dopant. The calculated value of ε' for undoped Sb_2Te_3 is 1516, while it is 397 and 236 for Sm- and In-doped Sb_2Te_3 microstructures, respectively. The lower value of ε' for SAT and IAT is related to the decrease in capacitance of grain boundaries, which confirms the enhancement of DC conductivity.[21]

Figure 5b shows the relation of the imaginary part of the permittivity dielectric loss (ε'') with increasing frequency. The graph depicts the gradual decrease in ε'' with increase in frequencies. This type of trend is well corelated to Deby's relaxation mechanism.[56] The loss is due to eddy current and defects that are created in the structure due to addition of the dopant. We observed lower value of dielectric loss in undoped Sb_2Te_3 microstructures, while higher values of ε'' were observed in the case of doped Sb_2Te_3 microstructures. The reason for Sm-doped Sb_2Te_3 microstructures showing a higher

https://doi.org/10.1021/acsomega.2c05859
ACS Omega 2023, 8, 9797−9806

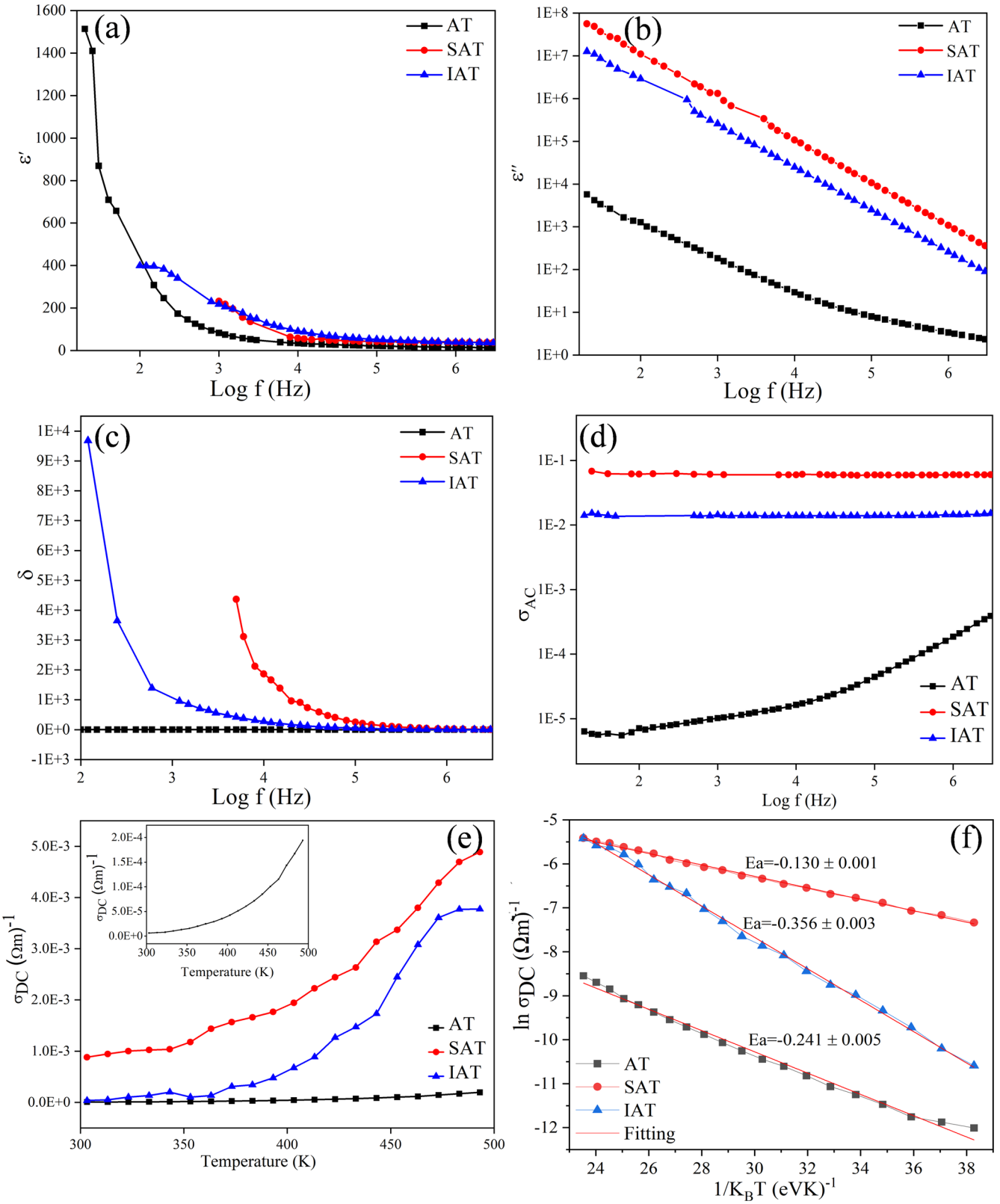

Figure 5. (a, b, c) Relation between the dielectric constant, dielectric loss, and tan loss of all prepared doped and undoped microstructures as a function of frequency; (d, e) temperature-based ac conductivities and dc conductivities; and (f) activation energies of all prepared doped and undoped Sb_2Te_3 microstructures.

value of dielectric loss for SAT and IAT is because rare earth elements are low-dielectric-loss materials.[54] Figure 5c shows the variation in tangent loss (Tan δ) as a function of frequency. Tan δ shows a similar trend with dielectric loss, as shown in Figure 5b. The tangent loss is directly proportional to the strain produced in the structure by doping. Addition of Sm and In as dopants is responsible for the generation of defects in the crystal structure, which leads to the origin of internal strain.[57]

https://doi.org/10.1021/acsomega.2c05859
ACS Omega 2023, 8, 9797−9806

IAT shows maximum tan δ because its crystallite size (42 nm) is smaller as compared to the crystallite size of Sm-doped (68 nm) and undoped Sb_2Te_3 microstructures (72 nm). The smaller the crystallite size, the more will be the internal strain, which will lead to a greater value of Tan δ.

2.5.2. Conductivity Studies. This section includes AC (σAC), DC (σDC), electrical conductivity, and thermal conductivity (κ) measurements of all prepared doped and undoped Sb_2Te_3 microstructures. Room-temperature AC conductivity was calculated as a function of frequency, while temperature-based DC conductivity measurements were carried out at 300−500 K. Thermal conductivity study was also done at variable temperature ranges from 298 to 393 K.

The relation of σ_{AC} with log f is provided in Figure 5d. This graph shows that σ_{AC} is directly related to log$f$. As the frequency increases, the value of σ_{AC} also increases, which can be explained by the jump relaxation model. According to this model, the phenomenon of ions or atom hopping is more prominent at lower frequencies, while at higher frequencies, the dispersion and relaxation process is more active. The successful hopping of ions or atoms (transfer of ions or atoms to some other lattice) is attributed to both AC and DC conductivities. But at higher frequencies, the process of unsuccessful hopping (ions or atoms hop, relax, reorient, and come back to their own lattice) is more obvious, which is responsible for the increase in the σ_{AC} value.[58] The undoped Sb_2Te_3 microstructure shows the usual trend of σ_{AC}, while SAT and IAT did not show eminent response toward the increase in frequency. Probably, this is due to the structural imperfections or defects in structure.[59] Although SAT and IAT did not give leading responses to increase in frequency, they have higher values of σ_{AC} as compared to their undoped counterparts.

Figure 5e shows the temperature-dependent DC conductivities (σ_{DC}) of doped and undoped Sb_2Te_3 microstructures. The DC conductivities of all prepared samples show a similar trend: an increase was observed with increase in temperature, which verifies the involvement of the thermally active transport mechanism in the conduction process.[60−63] As the temperature increases from 300 to 500 K, the movement of electrons becomes facile as they face less hindrance, so the higher DC conductivity was noticed. Further, we also observed an increment in the DC conductivity values of the doped Sb_2Te_3 microstructures. The observed DC conductivity values for SAT and IAT were 4.9×10^{-3} and 3.7×10^{-3} Ω^{-1} m^{-1}, which are higher than that of undoped Sb_2Te_3 microstructures, 1.92×10^{-4} Ω^{-1} m^{-1}. The effect of doping on the DC conductivity of Sb_2Te_3 microstructures can be explained by defect chemistry. When a heterovalent dopant is introduced in any material, it produces a disorder in their structure. Ultimately, in such a situation, charged disorders/defects are originated as a result of charged dopants. These charges on the defects were compensated by the formation of other defects having opposite charges. These compensation charges happen to occur either by reduction of positively charged species or by creation of holes[29,43] (electrons cannot be created by solvothermal methods; only holes can be created, which can be attributed as positive charges). Thus, the increase in electrical conductivities for SAT and IAT was attributed to the defects formed in their structures. Moreover, the addition of Sm and In doping also affects the crystallite size, as discussed in the structural analysis. The decrease in crystallite size is also responsible for the higher electrical conductivity.

The activation energies for the conductivities of doped and undoped Sb_2Te_3 microstructures were also calculated using Arrhenius relationship as given below.[44−47]

$$\sigma_{DC} = \sigma_{\circ} \exp\left(-\frac{E_a}{k_B T}\right)$$

where σ_{DC} is the electrical conductivity, $\sigma_{\circ}$ is the pre-exponential factor, E_a is the activation energy for conduction, and k_B is Boltzmann constant, having the value 1.380649×10^{-23} J K^{-1}. The value of activation energy for undoped Sb_2Te_3 was −0.24 eV, while the E_a values for SAT and IAT were −0.1304 and −0.356 eV, respectively, as provided in Figure 5f. The trend of activation energy depicts that the conduction of electrons is more facile in the case of Sm doping as compared to the In-doped Sb_2Te_3 microstructures. Therefore, the measured value of electrical conductivity for SAT is slightly high compared to IAT.

2.6. Thermal Transport Properties. To investigate the thermal transport behavior of the prepared materials, thermal conductivity (κ) and other related parameters were measured. The total thermal conductivity of the material is sum of electronic and lattice components, denoted by κ_e and κ_{ph}, respectively. The measured values of the thermal conductivity of doped and undoped Sb_2Te_3 microstructures are provided in Table 3. This data shows that the thermal conductivity of the

Table 3. Measured Values of the Thermal Conductivities of the Prepared AT, SAT, and IAT at 298 K

microstructures	thermal conductivity κ (W m^{-1} K^{-1})	thermal diffusivity α (mm^2 s^{-1})	volumetric specific heat capacity C (MJ m^{-3} K^{-1})
AT	0.68	0.33	2.07
SAT	0.63	0.74	0.84
IAT	0.60	0.25	2.39

Sb_2Te_3 microstructure decreases by addition of Sm and In. As discussed earlier, addition of the individual Sm or In dopant produces charged or point defects in the structure of Sb_2Te_3 that lead to enhanced phonon scattering. The increase in phonon scattering is mainly responsible for the decrease in thermal conductivity of the doped Sb_2Te_3 microstructures.[64] Moreover, the SAT and IAT have smaller crystallite sizes, as discussed earlier in the structural analysis. The smaller crystallites produce more interfaces, which also contributes to the increase of phonon scattering, ultimately leading to low thermal conductivity.[65] Therefore, owing to the smallest crystallite size, IAT shows the lowest κ value of 0.60 W m^{-1} K^{-1} compared to its other counterparts. Additionally, the temperature-dependent κ of all studied materials have been studied from 298 to 393 K. The obtained results show the regular trend of increase in κ with temperature up to 373 K, which becomes constant afterward, as shown in Figure 6. Besides that, no change in trend of κ was observed among AT, SAT, and IAT. IAT has the lowest value of κ (0.77 W m^{-1} K^{-1}) at 393 K as compared to AT (κ = 0.91 W m^{-1} K^{-1}) and SAT (κ = 0.82 W m^{-1} K^{-1}), similar to that observed at room temperature (298 K).

Furthermore, addition of dopants also affects the thermal diffusivity (α) and volumetric heat capacity (C) of prepared materials. As evident from the equation $\alpha = k/C$, there is a direct relationship between σ and κ, while they are inversely related with C.[66] Accordingly, AT and IAT show the regular

https://doi.org/10.1021/acsomega.2c05859
ACS Omega 2023, 8, 9797−9806

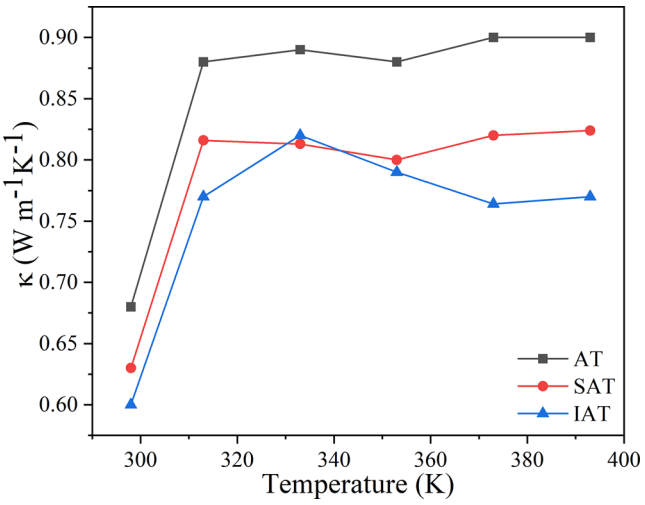

Figure 6. Temperature-dependent thermal conductivity κ of AT, SAT, and IAT.

behavior regarding thermal transport properties, while a higher value of thermal diffusivity (0.74 $mm^2 s^{-1}$) and lowest value of volumetric heat capacity (0.84 MJ $m^{-3} K^{-1}$) were observed in the case of SAT, which may be attributed to the difference in atomic masses of Sm and In, as the atomic mass/density of the material has a inverse relationship with *C*. Hence, Sm and In dopants certainly affect the thermal transport properties of Sb_2Te_3 microstructures, and these materials can be employed where a low thermal conductivity is needed, e.g. thermoelectric devices.

In addition, a broad comparison of all measured properties including dielectric constant, ac conductivity, temperature-dependent dc conductivity, and thermal conductivities of all studied materials AT, SAT, and IAT is provided in Table 4.

Table 4. Comparison of All Measured Parameters of AT, SAT, and IAT

sample type	dielectric constant ε'	AC conductivity $\sigma_{AC}\Omega^{-1}$ m^{-1}	DC conductivity $\sigma_{DC}\Omega^{-1}$ m^{-1}	thermal conductivity κ (W m^{-1} K^{-1})
AT	1517	3.88×10^{-4}	1.92×10^{-4}	0.68−0.91
SAT	397	0.01	4.9×10^{-3}	0.63−0.82
IAT	236	0.06	3.7×10^{-3}	0.60−0.77

We found a linear increment in σ_{AC} and σ_{DC} but decrease in ε' and κ by addition of Sm and In as dopants. Hence, we can deduce that Sm and In as dopants play a significant role in improvement of the conductivity behavior of Sb_2Te_3 microstructures. These results encourage us to deploy the prepared doped (SAT and IAT) materials in various energy-related applications where high electrical conductivity and low thermal conductivity are essential.

3. CONCLUSIONS

In summary, successful synthesis of undoped Sb_2Te_3 and Sm, and In-doped Sb_2Te_3 microstructures has been carried out by solvothermal synthesis. The detailed analyses verify the substitutional addition of Sm^{+3} and In^{+3} dopants within the lattice of Sb_2Te_3. The SEM micrographs, vibrational analysis, and TGA/DTA confirmed the uniform distribution of Sm and In within Sb_2Te_3 microstructures; moreover, doping did not shift the vibrational modes and thermal behavior of Sb_2Te_3 microstructures. The variation in dielectric parameters such as decrease in dielectric constant (1516−236), increase in dielectric loss, and tan loss were measured due to internal strain, and defects emerged because of Sm and In doping. An enhanced electrical conductivity of up to 0.06 Ω^{-1} m^{-1} was measured from frequency-based AC and temperature-based DC measurements, 4.9×10^{-3} Ω^{-1} m^{-1}. The activation energy calculations show the facile movement of electrons within doped Sb_2Te_3 microstructures, which facilitates the enhanced electrical conductivity. Further, the temperature-based thermal conductivity estimation shows a decrease in thermal conductivity by doping of Sm and In up to 0.60 W m^{-1} K^{-1} because of the phonon-scattering phenomena. Such improvement in electrical conductivity and decline in thermal conductivity suggest that trivalent Sm and In-doped Sb_2Te_3 microstructures can prove to be better candidates for thermoelectric and other electronic applications.

4. EXPERIMENTAL SECTION

4.1. Materials and Methods. All materials including $SmCl_3$, $InCl_3$, $SbCl_3$, $NaBH_4$, and Te powder purchased from Sigma Aldrich, having purity above 99%, were used without further purification.

4.2. Synthesis of (Sm, In)-Doped and Undoped Sb_2Te_3. Analytically pure metal (Sm) chloride (aq 0.1 mmol), antimony trichloride $SbCl_3$ (aq 2 mmol), tellurium powder (aq 3 mmol), and sodium borohydride (0.35 g) were added into a Teflon-lined autoclave having a capacity of 50 mL, as shown in Scheme 1. Subsequently, the autoclave was filled with a mixture of ethylenediamine and deionized water (8:2) up to 80% of its capacity. Afterwards, the autoclave was placed in a preheated oven and kept at a temperature of 433 K for 48 h. The autoclave was then cooled down to room temperature. The resulting precipitates were washed thrice with absolute alcohol and deionized water to remove any unreacted starting material. Finally, the washed precipitates were dried under vacuum at 343 K for 4 h. Further, the dried sample was annealed at 753 K under H_2/Ar mixture for 3 h to remove any oxide impurity.

Scheme 1. Solvothermal Synthesis of AT, SAT, and IAT Microstructures

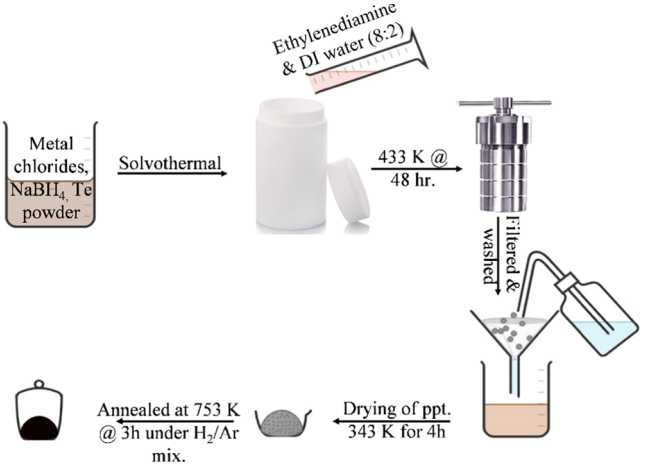

The undoped Sb_2Te_3 (AT) and indium-doped Sb_2Te_3 (IAT) were also synthesized by the same solvothermal process

https://doi.org/10.1021/acsomega.2c05859
ACS Omega 2023, 8, 9797−9806

except that during the synthesis of AT, only the salt of antimony trichloride ($SbCl_3$) was used.

AUTHOR INFORMATION

Corresponding Authors

Manzar Sohail − *Department of Chemistry, School of Natural Sciences (SNS), National University of Sciences and Technology (NUST), Islamabad 44000, Pakistan;* orcid.org/0000-0003-1457-2491; Email: manzar.sohail@sns.nust.edu.pk

Zahida Malik − *Department of Chemistry, School of Natural Sciences (SNS), National University of Sciences and Technology (NUST), Islamabad 44000, Pakistan;* Present Address: School of Chemistry, Faculty of Engineering and Physical Sciences, University of Southampton, Southampton SO17 1BJ, United Kingdom; Email: Zahida.malik63@yahoo.com

Authors

Nitasha Komal − *Department of Chemistry, School of Natural Sciences (SNS), National University of Sciences and Technology (NUST), Islamabad 44000, Pakistan*

Muhammad Adil Mansoor − *Department of Chemistry, School of Natural Sciences (SNS), National University of Sciences and Technology (NUST), Islamabad 44000, Pakistan*

Muhammad Mazhar − *Department of Chemistry, School of Natural Sciences (SNS), National University of Sciences and Technology (NUST), Islamabad 44000, Pakistan*

Muhammad Anis-ur-Rehman − *Applied Thermal Physics Laboratory, Department of Physics, COMSATS University Islamabad, Islamabad 44000, Pakistan;* orcid.org/0000-0003-3670-6892

Complete contact information is available at: https://pubs.acs.org/10.1021/acsomega.2c05859

Notes

The authors declare no competing financial interest.

ACKNOWLEDGMENTS

M.M., M.A.M., and N.K. are grateful to the Higher Education Commission of Pakistan for DNP, NRPU #20-12197/NRPU/R&D/HEC/2020, and indigenous research grants.

REFERENCES

(1) Ramasamy, K.; Gupta, R. K.; Sims, H.; Palchoudhury, S.; Ivanov, S.; Gupta, A. Layered ternary sulfide CuSbS2 nanoplates for flexible solid-state supercapacitors. *J. Mater. Chem. A* **2015**, *3*, 13263−13274.

(2) Poudeu, P. F. P.; Guéguen, A.; Wu, C. I.; Hogan, T.; Kanatzidis, M. G. High figure of merit in nanostructured n-type KPbmSbTe m+2 thermoelectric materials. *Chem. Mater.* **2010**, *22*, 1046−1053.

(3) Zhou, M.; Li, J. F.; Kita, T. Nanostructured AgPbmSbTem+2 system bulk materials with enhanced thermoelectric performance. *J. Am. Chem. Soc.* **2008**, *130*, 4527−4532.

(4) Xu, D.; Shen, S.; Zhang, Y.; Gu, H.; Wang, Q. Selective Synthesis of Ternary Copper − Antimony Sul fi de Nanocrystals. *Inorg. Chem.* **2013**, *52*, 12958−12962.

(5) Jang, W.; Lee, J.; In, C.; Choi, H.; Soon, A. Designing Two-Dimensional Dirac Heterointerfaces of Few-Layer Graphene and Tetradymite-Type Sb2Te3 for Thermoelectric Applications. *ACS Appl. Mater. Interfaces* **2017**, *9*, 42050−42057.

(6) Kim, J. H.; Choi, J. Y.; Bae, J. M.; Kim, M. Y.; Oh, T. S. Thermoelectric Characteristics of n-Type Bi2Te3 and p-Type Sb2Te3 Thin Films Prepared by Co-Evaporation and Annealing for Thermopile Sensor Applications. *Mater. Trans.* **2013**, *54*, 618−625.

(7) Zhu, M.; Wu, L.; Rao, F.; Song, Z.; Ren, K.; Ji, X.; Song, S.; Yao, D.; Feng, S. Uniform Ti-doped Sb2Te3 materials for high-speed phase change memory applications. *Appl. Phys. Lett.* **2014**, *104*, No. 053119.

(8) Lewin, M.; Mester, L.; Saltzmann, T.; Chong, S. J.; Kaminski, M.; Hauer, B.; Pohlmann, M.; Mio, A. M.; Wirtssohn, M.; Jost, P.; Wuttig, M.; et al. Sb2Te3 Growth Study Reveals That Formation of Nanoscale Charge Carrier Domains Is an Intrinsic Feature Relevant for Electronic Applications. *ACS Appl. Nano Mater.* **2018**, *1*, 6834−6842.

(9) Zhang, Z.; Zhang, H.; Wu, Y.; Zeng, Z.; Hu, Z. Optimization of the thermopower of antimony telluride thin film by introducing tellurium nanoparticles. *Appl. Phys., A* **2015**, *118*, 1043−1051.

(10) Stavila, V.; Robinson, D. B.; Hekmaty, M. A.; Nishimoto, R.; Medlin, D. L.; Zhu, S.; Tritt, T. M.; Sharma, P. A. Wet-chemical synthesis and consolidation of stoichiometric bismuth telluride nanoparticles for improving the thermoelectric figure-of-merit. *ACS Appl. Mater. Interfaces* **2013**, *5*, 6678−6686.

(11) Ganguly, S.; Zhou, C.; Morelli, D.; Sakamoto, J.; Uher, C.; Brock, S. L. Synthesis and evaluation of lead telluride/bismuth antimony telluride nanocomposites for thermoelectric applications. *J. Solid State Chem.* **2011**, *184*, 3195−3201.

(12) Gasenkova, I. V.; Ivanova, L. D.; Granatkina, Y. V. Structural defects in tin-doped antimony telluride single crystals. *Inorg. Mater.* **2001**, *37*, 1112−1117.

(13) Mehta, R. J.; Zhang, Y.; Zhu, H.; Parker, D. S.; Belley, M.; Singh, D. J.; Ramprasad, R.; Borca-Tasciuc, T.; Ramanath, G. Seebeck and figure of merit enhancement in nanostructured antimony telluride by antisite defect suppression through sulfur doping. *Nano Lett.* **2012**, *12*, 4523−4529.

(14) Kumari, M.; Sharma, Y. C. Effect of doping with "se" on structural, optical, electrical and thermoelectric properties of multi-layers of $Bi_2Te_{2.7}Se_{0.3}/Sb_2Te_3$ to enhance thermoelectric performance. *Nanosyst.: Phys., Chem., Math.* **2019**, *10*, 686−693.

(15) Nielsen, M. D.; Jaworski, C. M.; Heremans, J. P. Off-stoichiometric silver antimony telluride: An experimental study of transport properties with intrinsic and extrinsic doping. *AIP Adv.* **2015**, *5*, No. 053602.

(16) Das, D.; Malik, K.; Deb, A. K.; Kulbachinskii, V. A.; Kytin, V. G.; Chatterjee, S.; Das, D.; Dhara, S.; Bandyopadhyay, S.; Banerjee, A. Tuning of thermoelectric properties with changing Se content in Sb2Te3. *EPL (Europhys. Lett.)* **2016**, *113*, No. 47004.

(17) Ding, K.; Rao, F.; Xia, M.; Song, Z.; Wu, L.; Feng, S. The impact of W doping on the phase change behavior of Sb2Te3. *J. Alloys Compd.* **2016**, *688*, 22−26.

(18) Ji, X.; Wu, L.; Cao, L.; Zhu, M.; Rao, F.; Zheng, Y.; Zhou, W.; Song, Z.; Feng, S. Vanadium doped Sb2Te3 material with modified crystallization mechanism for phase-change memory application. *Appl. Phys. Lett.* **2015**, *106*, No. 243103.

(19) Fan, P.; Chen, T.; Zheng, Z.; Zhang, D.; Cai, X.; Cai, Z.; Huang, Y. The influence of Bi doping in the thermoelectric properties of co-sputtering deposited bismuth antimony telluride thin films. *Mater. Res. Bull.* **2013**, *48*, 333−336.

(20) Thankamma, G.; Kunjomana, A. G. Studies on sulfur doping and figure of merit in vapor grown Sb2Te3 platelet crystals. *J. Cryst. Growth* **2015**, *415*, 65−71.

(21) Yotburut, B.; Thongbai, P.; Yamwong, T.; Maensiri, S. Synthesis and characterization of multiferroic Sm-doped BiFeO3 nanopowders and their bulk dielectric properties. *J. Magn. Magn. Mater.* **2017**, *437*, 51−61.

(22) Sharma, K.; Al-Kabbi, A. S.; Saini, G. S. S.; Tripathi, S. K. Indium doping induced modification of the structural, optical and electrical properties of nanocrystalline CdSe thin films. *J. Alloys Compd.* **2013**, *564*, 42−48.

(23) Aghazadeh, M.; Ganjali, M. R. Samarium-doped Fe3O4 nanoparticles with improved magnetic and supercapacitive performance: a novel preparation strategy and characterization. *J. Mater. Sci.* **2018**, *53*, 295−308.

(24) Faraz, M.; Naqvi, F. K.; Shakir, M.; Khare, N. Synthesis of samarium-doped zinc oxide nanoparticles with improved photocatalytic performance and recyclability under visible light irradiation. *New J. Chem.* **2018**, *42*, 2295−2305.
(25) Bao, H.; Du, M.; Wang, H.; Wang, K.; Zuo, X.; Liu, F.; Liu, L.; Eder, D.; Cherevan, A.; Wang, S.; Wan, L.; et al. Samarium-Doped Nickel Oxide for Superior Inverted Perovskite Solar Cells: Insight into Doping Effect for Electronic Applications. *Adv. Funct. Mater.* **2021**, *31*, No. 2102452.
(26) Atayeva, S. U.; Mekhtiyeva, S. I.; Isayev, A. I. Dispersion of the refractive index of a samarium-doped Se95Te5 chalcogenide glassy semiconductor. *Semiconductors* **2015**, *49*, 949−952.
(27) Alekberov, R. I.; Isayev, A. I.; Mekhtiyeva, S. I. Features of Raman scattering and X-ray diffraction in As-Se-Te (S) chalcogenide glasses doped by samarium. *Mol. Cryst. Liq. Cryst.* **2021**, *717*, 24−31.
(28) Tahir, M.; Amin, N. S. Indium-doped TiO2 nanoparticles for photocatalytic CO2 reduction with H2O vapors to CH4. *Appl. Catal., B* **2015**, *162*, 98−109.
(29) Chava, R. K.; Kang, M. Improving the photovoltaic conversion efficiency of ZnO based dye sensitized solar cells by indium doping. *J. Alloys Compd.* **2017**, *692*, 67−76.
(30) Prabhu, M.; Marikkannan, M.; Pandian, M. S.; Ramasamy, P.; Ramachandran, K. Effect of zinc and indium doping in chalcogenide (CdS/Te) nanocomposites towards dye-sensitized solar cell applications. *J. Phys. Chem. Solids* **2022**, *168*, No. 110802.
(31) Xia, Y.; Bian, X.; Xia, Y.; Zhou, W.; Wang, L.; Fan, S.; Xiong, P.; Zhan, T.; Dai, Q.; Chen, J. Effect of indium doping on the PbO2 electrode for the enhanced electrochemical oxidation of aspirin: An electrode comparative study. *Sep. Purif. Technol.* **2020**, *237*, No. 116321.
(32) Qi, J.; Zhang, H.; Lu, S.; Li, X.; Xu, M.; Zhang, Y. High performance indium-doped ZnO gas sensor. *J. Nanomater.* **2015**, *16*, No. 74.
(33) Pati, S.; Banerji, P.; Majumder, S. B. Properties of indium doped nanocrystalline ZnO thin films and their enhanced gas sensing performance. *RSC Adv.* **2015**, *5*, 61230−61238.
(34) Elkatlawy, S. M.; El-Dosokey, A. H.; Gomaa, H. M. Structural properties, linear, and non-linear optical parameters of ternary Se80Te(20−x)Inx chalcogenide glass systems. *Bol. Soc. Esp. Ceram. Vidrio* **2022**, *61*, 203−209.
(35) Wu, L.; Li, X.; Wang, S.; Zhang, T.; Yang, J.; Zhang, W.; Chen, L.; Yang, J. Resonant level-induced high thermoelectric response in indium-doped GeTe. *NPG Asia Mater.* **2017**, *9*, No. e343.
(36) Cheng, Y.; Yang, J.; Jiang, Q.; Fu, L.; Xiao, Y.; Luo, Y.; Zhang, D.; Zhang, M. CuCrSe2 Ternary Chromium Chalcogenide: Facile Fabrication, Doping and Thermoelectric Properties. *J. Am. Ceram. Soc.* **2015**, *98*, 3975−3980.
(37) Ferrer-Argemi, L.; Yu, Z.; Kim, J.; Myung, N. V.; Lim, J. H.; Lee, J. Silver content dependent thermal conductivity and thermoelectric properties of electrodeposited antimony telluride thin films. *Sci. Rep.* **2019**, *9*, No. 9242.
(38) Shi, D.; Wang, R.; Wang, G.; Li, C.; Shen, X.; Nie, Q. Enhanced thermoelectric properties in Cu-doped Sb2Te3 films. *Vacuum* **2017**, *145*, 347−350.
(39) Anis-ur-Rehman, M.; Maqsood, A. A modified transient method for an easy and fast determination of thermal conductivities of conductors and insulators. *J. Phys. D: Appl. Phys.* **2002**, *35*, No. 2040.
(40) Harris RITDC. tagami Lake, Quebec, and is to be applied to 197312, pp 1−6.
(41) Nithiyanantham, U.; Ede, S. R.; Ozaydin, M. F.; Liang, H.; Rathishkumar, A.; Kundu, S. Low temperature, shape-selective formation of Sb2Te3 nanomaterials and their thermoelectric applications. *RSC Adv.* **2015**, *5*, 89621−89634.
(42) Garje, S. S.; Eisler, D. J.; Ritch, J. S.; Afzaal, M.; O'Brien, P.; Chivers, T. A new route to antimony telluride nanoplates from a single-source precursor. *J. Am. Chem. Soc.* **2006**, *128*, 3120−3121.
(43) Poudel, B.; Hao, Q.; Ma, Y.; Lan, Y.; Minnich, A.; Yu, B.; Yan, X.; Wang, D.; Muto, A.; Vashaee, D.; Chen, X.; Liu, J.; Dresselhaus, M. S.; Chen, G.; Ren, Z. High-Thermoelectric Performance of Nanostructured Bismuth Antimony Telluride Bulk Alloys. *Science* **2008**, *320*, 634−638.
(44) Benouis, C. E.; Benhaliliba, M.; Sanchez Juarez, A.; Aida, M. S.; Chami, F.; Yakuphanoglu, F. The effect of indium doping on structural, electrical conductivity, photoconductivity and density of states properties of ZnO films. *J. Alloys Compd.* **2010**, *490*, 62−67.
(45) Jayanthi, K.; Chawla, S.; Sood, K. N.; Chhibara, M.; Singh, S. Dopant induced morphology changes in ZnO nanocrystals. *Appl. Surf. Sci.* **2009**, *255*, 5869−5875.
(46) Shahil, K. M. F.; Hossain, M. Z.; Goyal, V.; Balandin, A. A. Micro-Raman spectroscopy of mechanically exfoliated few-quintuple layers of Bi_2Te_3, Bi_2Se_3, and Sb_2Te_3 materials. *J. Appl. Phys.* **2012**, *111*, No. 054305.
(47) Komaraiah, D.; Radha, E.; James, J.; Kalarikkal, N.; Sivakumar, J.; Ramana Reddy, M. V.; Sayanna, R. Effect of particle size and dopant concentration on the Raman and the photoluminescence spectra of TiO_2 :Eu^{3+} nanophosphor thin films. *J. Lumin.* **2019**, *211*, 320−333.
(48) Kelly, S.; Pollak, F. H.; Tomkiewicz, M. Raman Spectroscopy as a Morphological Probe for TiO2 Aerogels. *J. Phys. Chem. B* **1997**, *101*, 2730−2734.
(49) Wu, Z.; Chen, X.; Mu, E.; Liu, Y.; Che, Z.; Dun, C.; Sun, F.; Wang, X.; Zhang, Y.; Hu, Z. Lattice Strain Enhances Thermoelectric Properties in Sb2Te3/Te Heterostructure. *Adv. Electron Mater.* **2020**, *6*, No. 1900735.
(50) Cody, C. A.; Dlcarlo, L.; Darlington, R. K. Vibrational and Thermal Study of Antimony Oxides. *Inorg. Chem.* **1979**, *18*, 1572−1576.
(51) Shi, J.; Chen, X.; Wang, W.; Chen, H. A new rapid synthesis of thermoelectric Sb2Te3 ingots using selective laser melting 3D printing. *Mater. Sci. Semicond. Process.* **2021**, *123*, No. 105551.
(52) Niu, L.; Xu, J.; Yang, W.; Zhao, J.; Su, J.; Guo, Y.; Liu, X. Research on nano-Sb2O3 flame retardant in char formation of PBT. *Ferroelectrics* **2018**, *523*, 14−21.
(53) Qu, H.; Wu, W.; Zheng, Y.; Xie, J.; Xu, J. Synergistic effects of inorganic tin compounds and Sb2O3 on thermal properties and flame retardancy of flexible poly(vinyl chloride). *Fire Saf. J.* **2011**, *46*, 462−467.
(54) Al-Hilli, M. F.; Li, S.; Kassim, K. S. Structural analysis, magnetic and electrical properties of samarium substituted lithiumnickel mixed ferrites. *J. Magn. Magn. Mater.* **2012**, *324*, 873−879.
(55) Kamran, M.; Anis-ur-Rehman, M. Enhanced transport properties in Ce doped cobalt ferrites nanoparticles for resistive RAM applications. *J. Alloys Compd.* **2020**, *822*, No. 153583.
(56) Ateia, E.; Ahmed, M. A.; El-Aziz, A. K. Effect of rare earth radius and concentration on the structural and transport properties of doped Mn-Zn ferrite. *J. Magn. Magn. Mater.* **2007**, *311*, 545−554.
(57) Narang, S. B.; Kaur, D.; Pubby, K. Effect of Substitution of Samarium and Lanthanum on Dielectric and Electrical Properties of Barium Titanate. *Ferroelectrics* **2015**, *486*, 74−85.
(58) Toor, R.; Anis-ur-Rehman, M. Facile Synthesis and Conductivity Studies of Multifunctional [CGN]/[LNS] Composite Material as Relaxor Dielectric. *J. Mater. Sci.: Mater. Electron.* **2019**, *30*, 2669−2681.
(59) Komal, N.; Malik, Z.; Ali, N. Z.; Chaudhary, A. J. Synthesis, characterization and properties of hierarchically assembled antimony oxyhalides nanonetworks. *Mater. Res. Express* **2019**, *6*, No. 065035.
(60) Triyono, D.; Fitria, S. N.; Hanifah, U. Dielectric analysis and electrical conduction mechanism of La1−xBixFeO3ceramics. *RSC Adv.* **2020**, *10*, 18323−18338.
(61) Kumar, P.; Presto, S.; Sinha, A. S. K.; Varma, S.; Viviani, M.; Singh, P. Effect of samarium (Sm3+) doping on structure and electrical conductivity of double perovskite Sr2NiMoO6 as anode material for SOFC. *J. Alloys Compd.* **2017**, *725*, 1123−1129.
(62) Kahlaoui, M.; Chefi, S.; Inoubli, A.; Madani, A.; Chefi, C. Synthesis and electrical properties of co-doping with La3+, Nd3+, Y3+, and Eu3+ citric acid-nitrate prepared samarium-doped ceria ceramics. *Ceram. Int.* **2013**, *39*, 3873−3879.

https://doi.org/10.1021/acsomega.2c05859
ACS Omega 2023, 8, 9797−9806

(63) Yao, Y. B.; Liu, W. C.; Mak, C. L. Pyroelectric properties and electrical conductivity in samarium doped BiFeO3 ceramics. *J. Alloys Compd.* **2012**, *527*, 157−162.
(64) Satyala, N.; Vashaee, D. The effect of crystallite size on thermoelectric properties of bulk nanostructured magnesium silicide (Mg 2Si) compounds. *Appl. Phys. Lett.* **2012**, *100*, No. 073107.
(65) Ngo, T. N. M.; Palstra, T. T. M.; Blake, G. R. Crystallite size dependence of thermoelectric performance of CuCrO2. *RSC Adv.* **2016**, *6*, 91171−91178.
(66) Ochsner, T. E.; Horton, R.; Ren, T. A New Perspective on Soil Thermal Properties. *Soil Sci. Soc. Am. J.* **2001**, *65*, 1641−1647.

https://doi.org/10.1021/acsomega.2c05859
ACS Omega 2023, 8, 9797−9806